Salt-fingering convection in the small diffusivity ratio limit

Jin-Han Xie[1], Benjamin Miquel[2], Edgar Knobloch[1] and Keith Julien[2]

[1]Department of Physics,
University of California at Berkeley
[2]Department of Applied Mathematics,
University of Colorado at Boulder
j.h.xie@berkeley.edu

Abstract

Doubly diffusive processes play a fundamental role in many physical phenomena of substantial geophysical and astrophysical importance. Despite much research basic questions, e.g. how primary and secondary instabilities saturate and how mean fields are generated, remain unresolved. In the salt-finger regime, we use a systematic asymptotic procedure to reduce the primitive equations to a prognostic equation for the evolution of the salinity field coupled to a novel diagnostic relation between the salinity and streamfunction. The reduced model preserves both the linear and nonlinear properties of the original system including primary and secondary instabilities and the establishment of a statistically steady saturated state. We identify the flux spectrum as a good diagnostic for the presence of salt fingers: in the horizontal spectrum, we find two distinctive scaling laws whose ranges are separated by the optimal wavenumber, while a Gaussian distribution is discovered for the vertical spectrum.

1 Introduction

Doubly diffusive systems in which two components with different diffusivities contribute to buoyancy in opposite ways arise frequently in geophysics and astrophysics (Turner, 1974; Schmitt, 1994). For example, doubly diffusive mixing is triggered in the ocean whenever a destabilizing slower diffuser (salinity) competes with a stabilizing faster diffuser (temperature). In giant planets as well as in massive stars, an unstable fast diffuser (temperature) and stable slow diffuser (composition) are responsible for important mixing processes. In this paper we concentrate on the former case. This case leads to salt-fingering convection.

Linear stability properties of the salt-finger regime were first determined by Stern (1960). As the magnitude of the unstable mode grows secondary instabilities are triggered (Holyer, 1984), and finally lead to a statistically steady state (Shen, 1995; Radko, 2010). However, the physical processes behind the presence of such an equilibrium state are still incompletely understood. Stern (1969) has suggested that a collective instability can lead to the disruption of the salt-finger field and lead to saturation, and identified a dimensionless quantity, now called the Stern number, that can be used as a criterion for saturation. Others have supposed that saturation will arise once the growth rate of a secondary instability, such as those identified by Holyer (1984), becomes comparable to that of the salt-finger instability (Radko and Smith, 2012).

Except for weakly nonlinear approaches, eg., Proctor and Holyer (1986); Radko (2010), most researches employ numerical studies of the full system. Such studies, particular in three dimensions, have proved invaluable and identified a number of novel processes, eg., Traxler et al. (2011). To shed light on some of these we propose here a semi-analytic

procedure that leads to a simplified set of equations that are easier to study, both theoretically and numerically. In the following we refer to these equations as the reduced equations, cf. Julien and Knobloch (2007). The procedure described below focuses on the double limit of a large density ratio and a small diffusivity ratio and leads to a reduced model with a prognostic-diagnostic form. To demonstrate the procedure we limit ourselves to two spatial dimensions. We present our derivation in §2, discuss secondary instabilities and the properties of the saturated state within the reduced system in §3 and §4, followed by conclusions in §5.

2 Model derivation

We start from the dimensionless equations describing warm salty fluid overlying cool fresh fluid in two dimensions:

$$\frac{1}{\mathrm{Pr}}\left[\frac{\partial}{\partial t}\nabla^2\psi + \mathcal{J}\left(\psi,\nabla^2\psi\right)\right] = \frac{\partial T}{\partial x} - \frac{\partial S}{\partial x} + \nabla^4\psi, \tag{1a}$$

$$\frac{\partial}{\partial t}T + \mathcal{J}\left(\psi,T\right) + \frac{\partial \psi}{\partial x} = \nabla^2 T, \tag{1b}$$

$$\frac{\partial}{\partial t}S + \mathcal{J}\left(\psi,S\right) + \frac{1}{\mathrm{R}_\rho}\frac{\partial \psi}{\partial x} = \tau\nabla^2 S. \tag{1c}$$

Here ψ is the streamfunction such that $\boldsymbol{u} = \nabla^\perp\psi$, T is the temperature field, S is the salinity field, Pr is the Prandtl number, R_ρ is the density ratio and τ is the ratio of the diffusivities of salinity and temperature. The symbol $\mathcal{J}\left(a,b\right)$ denotes $a_x b_z - a_z b_x$ with x and z the horizontal and vertical directions, respectively. These equations have been nondimensionalized using the natural salt-finger scale (Radko, 2010). As a result the parameter regime of interest is $\mathrm{R}_\rho > 1$ and $\tau < 1$ so that the system is convectively stable but unstable due to the different diffusivities of the competing fields. The trivial (conduction) state of this system is linearly unstable when $1 < \mathrm{R}_\rho < \tau^{-1}$. The system also possesses a family of *exact* elevator-mode solutions in the form of $(\psi, T, S) = \Re\left\{(\psi_e, T_e, S_e)\mathrm{e}^{\mathrm{i}kx}\right\}$. These solutions are independent of the vertical coordinate z and are present for any amplitude, i.e., no nonlinear saturation of these states takes place.

In the following we focus on the small diffusivity ratio limit of this system by introducing a small parameter $\epsilon \ll 1$ such that $\tau = \epsilon\tilde{\tau}$ with $\tilde{\tau} = O(1)$. In the context of thermohaline problem this limit is physically sound since $\tau \approx 0.01$. Next, we take $\mathrm{R}_\rho = \epsilon^{-1}\tilde{\mathrm{R}}_\rho$, meaning that the stabilizing temperature gradient is much stronger than the destabilizing salinity gradient. This is an interesting regime to consider since the destabilizing effect of the salinity stratification is pushed beyond the leading order, leading to important simplification. In addition, we introduce the following scaling of the dependent fields

$$\psi = \epsilon\tilde{\psi}, \qquad T = \epsilon\tilde{T}, \qquad S = \epsilon\tilde{S} \tag{2}$$

and focus on the low Prandtl number limit $\mathrm{Pr} = \epsilon\widetilde{\mathrm{Pr}}$.

In terms of the slow time $\tilde{t} \equiv \epsilon t$ these assumptions yield the following leading order equations

$$\frac{1}{\mathrm{Pr}}\left[\frac{\partial}{\partial t}\nabla^2\psi + \mathcal{J}\left(\psi,\nabla^2\psi\right)\right] = -\frac{\partial S}{\partial x} + \left(\nabla^4 + \Delta^{-1}\partial_x^2\right)\psi, \tag{3a}$$

$$\frac{\partial}{\partial t}S + \mathcal{J}\left(\psi,S\right) + \frac{1}{\mathrm{R}_\rho}\frac{\partial \psi}{\partial x} = \tau\nabla^2 S, \tag{3b}$$

where for simplicity we omitted the $\tilde{}$ decoration. Note that the leading order T equation degenerates to a constraint, $\psi_x = \nabla^2 T$, which is applied to eliminate T from Eqs. (3). Note that by rescaling and changing the variable S to $-\theta$ Eqs. (3) can be written as a Rayleigh-Bénard convection (RBC) system with additional vorticity dissipation given by $\Delta^{-1}\partial_x^2\psi$. Since this new dissipation is stronger for larger scale structures, with suitable boundary condition the optimal mode that has the largest growth rate has a finite characteristic scale in the horizontal, in contrast to RBC where the scale of the optimal mode depends on the domain size. Thus the temperature field is responsible for the introduction of large-scale damping.

A further reduction is achieved by taking the scaled Prandtl number to be large and normalizing ψ, S and ∂_t by τ, resulting in the prognostic-diagnostic model

$$\frac{\partial}{\partial t}S + \mathcal{J}\left(\psi, S\right) + \mathrm{Ra}\frac{\partial \psi}{\partial x} = \nabla^2 S, \qquad \left(\nabla^6 + \partial_x^2\right)\psi = \partial_x \nabla^2 S, \tag{4}$$

where $\mathrm{Ra} = 1/(\mathrm{R}_\rho \tau)$. Evidently the dynamics of this model only depend on the single physical parameter Ra and the domain size. The prognostic form of this model is interesting in the geophysical flow context, where β-plane vorticity dynamics, Bénard convection in the large Prandtl number limit and β-convection all share the same form.

Together with the diagnostic relation we can interpret the physics of the linear instability as follows. The diagnostic relation requires that the ψ and S fields are out-of-phase implying that the local maximum (minimum) of the perturbation of S tends to increase (decrease) as time increases. The competition between this amplifying mechanism and dissipation determines stability and results in the criterion $\mathrm{Ra} > 1$ for instability, an identical condition to that for the original system (1).

It is easy to check that the elevator modes remain solutions of the reduced model, including that with the optimum wavenumber

$$k_{\mathrm{opt}}^4 = \frac{1}{2}\left(-2 - \mathrm{Ra} + \sqrt{\mathrm{Ra}^2 + 8\mathrm{Ra}}\right) \quad \text{and} \quad m = 0. \tag{5}$$

However, the utility of the reduced system (4) extends beyond linear stability properties since it also captures the nonlinear effects arising from advection, a process that is crucial for the saturation of the growing salt fingers.

Our reduced model (4) turns out to be similar to the weakly nonlinear model derived by Radko (2010) (see Eqs. (8) and (11) of Radko (2010)). Even though different parameter regimes are considered in the two models – our reduced model captures the regime where linear dynamics is not confined to the onset of instability (Ra ranges from 1 to ∞) in the limit of small τ, while the Radko (2010) model relaxes the small τ assumption but is restricted to dynamics near the onset – the two models match in the overlapping regime $\tau \ll 1$ and $\mathrm{Ra} = 1 + \epsilon R$ with $\epsilon \ll 1$ and $R = O(1)$. In this regime, the optimal scale from Eq. (5) is $O(\epsilon^{-1/4})$ suggesting the rescaling

$$\partial_t \to \epsilon^{9/4}\partial_t, \quad \nabla \to \epsilon^{1/4}\nabla, \quad \psi \to \epsilon\psi \quad \text{and} \quad S \to \epsilon^{3/4}S. \tag{6}$$

With this rescaling the leading order contribution to (4) reads

$$\partial_t S + \mathcal{J}\left(\frac{\nabla^2}{\partial_x}S, S\right) + \left(R - \frac{\nabla^6}{\partial_x^2}\right)\nabla^2 S = 0, \tag{7}$$

which is identical to the Radko (2010) model in the limit of small τ.

3 Secondary instabilities

Following Holyer (1984), we analyze the secondary instability of steady salt fingers by means of single vertical mode Floquet theory and compare the growth rate calculated from our reduced models (4) and (3) with that computed from the original system (1). Floquet theory considers perturbations of the form

$$\begin{pmatrix}\psi\\ S\end{pmatrix} = \mathrm{e}^{\alpha t+\mathrm{i}k(px+qz)} \sum_{n=-N}^{n=N} \begin{pmatrix}\psi_n\\ \mathrm{i}S_n\end{pmatrix} \mathrm{e}^{\mathrm{i}nkx}. \tag{8}$$

For the reduced model (4), we take Ra = 1.1 and assume that the salt finger field has amplitude $S_\mathrm{e} = 6.5$ as obtained from Fig. 1(d) and is stationary. For the modified RBC system (3), the parameters are chosen to be $\tau = 1$, $1/\mathrm{R}_\rho = 1.1$ and $\mathrm{Pr} = 10^4$, and $S_\mathrm{e} = 6.5$ as well. The results obtained are compared with the corresponding results for the primitive system (1) with $\tau = 0.01$, $1/\mathrm{R}_\rho = 0.011$ and $\mathrm{Pr} = 1$, and correspondingly $S_\mathrm{e} = 0.065$. We show a contour plot of the growth rate α as a function of p and q in Fig. 1. The observed match between the first three panels demonstrates that the validity of the reduced models extends far into the nonlinear regime. In the last panel we show the salinity field obtained from a simulation of the reduced model (4) with an initial condition that is a combination of the optimal mode and superposed small random noise. The figure shows that at $t = 180$ the secondary instability sets in with a vertical wavenumber comparable to that of the optimal mode, an observation that is well explained by the single vertical mode Floquet theory which predicts that the largest growth rate occurs for $p = 0$ and $q = 1.05$ obtained from Floquet theory with $S_\mathrm{e} = 6.5$. These results should be compared with those of Stern and Simeonov (2005) for $\mathrm{Pr} = 7$, $\mathrm{R}_\rho = 2$ and $\tau = 1/24$, for which the secondary instability sets in with vertical wavenumber of 0.8 times optimal wavenumber. Both results confirm the validity of the single vertical mode Floquet theory in triggering the secondary instability.

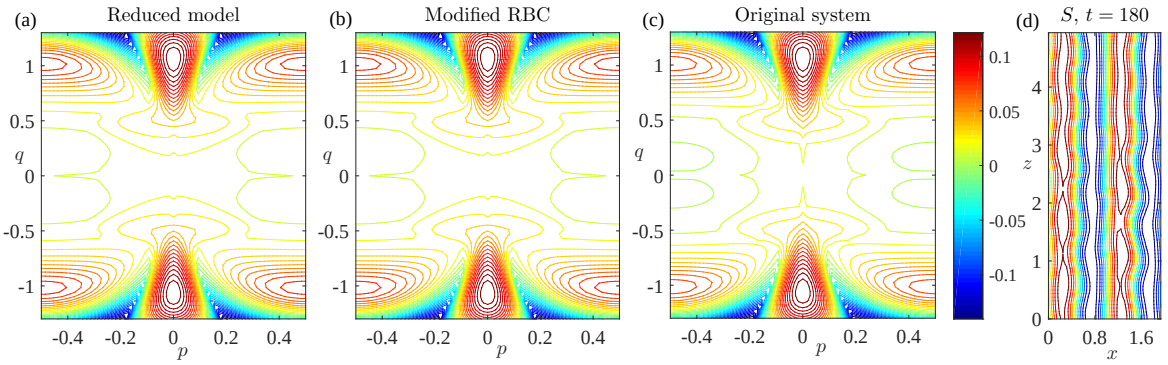

Figure 1: Contours of constant growth rate α in the (p, q) plane for (a) the reduced model (4), (b) the modified RBC equations (3) and (c) the primitive system (1). (d) The salinity field in the early stage ($t = 180$) of the secondary instability in a 2×5 domain in units of the optimal mode wavelength. Wavenumbers are normalized by the optimal wavenumber given by (5).

4 Saturated state

In this section we describe the results of simulations for Ra = 1.1 in a doubly periodic domain with different domain sizes. For this value of Ra, the large optimal scale distinguishes our reduced model from Bénard convection in the large Prandtl number limit.

In particular, our reduced model (4) differs from (7) when anisotropic structures with horizontal scales much larger than the vertical scale are considered.

In Fig. 2, we show the dynamics in a domain of size 1×2 in units of the optimal wavelength, defined as $2\pi/k_{\rm opt}$, obtained from an initial condition in which S takes the form of a random field with zero x average. Panel (a) shows that the total energy $E_S = (1/2)\int S^2 \mathrm{d}x\mathrm{d}z$ reaches a steady state. Properties of this state are shown in panels (b) and (c) in terms of salinity field at large times and the corresponding horizontal mean flow, respectively. These results are characteristic of small domain dynamics.

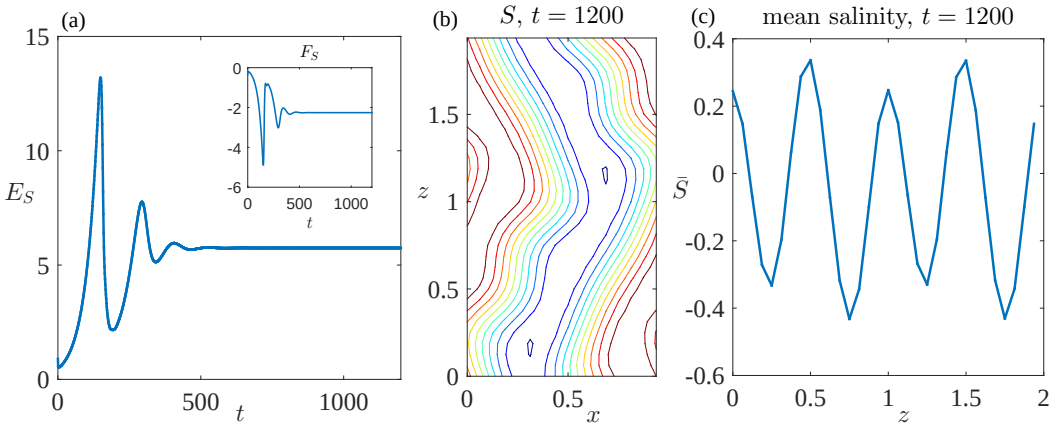

Figure 2: Results from a small-domain simulation. (a) Evolution of the total energy with time. (b) Large-time salinity field. (c) Associated horizontal mean flow with z now plotted along the horizontal axis. Distances are measured in units of the wavelength of the optimal mode.

With increasing domain size the system exhibits irregular bursts, much as observed in Traxler et al. (2011) (not shown). When the domain becomes even larger, a statistically steady state is reached. To illustrate this result we show in Fig. 3 the results obtained in a domain of size 32×32 in units of the optimal wavelength starting from an initial condition in the form of a constant amplitude salt finger field with a small amplitude random field superposed. We ran the simulation to $t = 4800$ and observed (Fig. 3(a)) that a statistically steady state is reached.

Three stages toward saturation can be identified: (i) Dominance of salt fingers. This is the stage corresponding to peak energy and flux generation. Fig. 3(b) shows the salinity field in the vicinity of this peak ($t \approx 180$); long finger structures are observed. (ii) Secondary instabilities. The salt fingers cannot grow without bound owing to the onset of secondary instability, whose growth rate increases with the amplitude of the growing of salt-finger as discussed in detail in the previous section. (iii) In the final saturation stage no balance between the growth rate of a particular secondary instability and the growth rate of the salt fingers has been identified. This regime is characterized by collisions of upward and downward fingers Shen (1995) and it appears that it is a combination of these two effects – secondary instability and salt finger collision – that is responsible for the observed statistically steady saturated state. Fig. 3(c) provides a snapshot of the final statistically steady salinity field. Finger-like structures can still be recognized but these are of small spatial extent and quite different from stage (i).

We pay special attention to the statistically steady state. In Fig. 4(a) we show the spectral energy input defined as $\lambda(k,m)|\hat{S}|$ with λ the growth rate and $\hat{\cdot}$ denoting the Fourier transform. This quantity is derived from the energy budget, viz. $\mathrm{d}E_S/\mathrm{d}t = \int \lambda(k,m)|\hat{S}|\mathrm{d}k\mathrm{d}m$. The figure shows that the energy input concentrates around the opti-

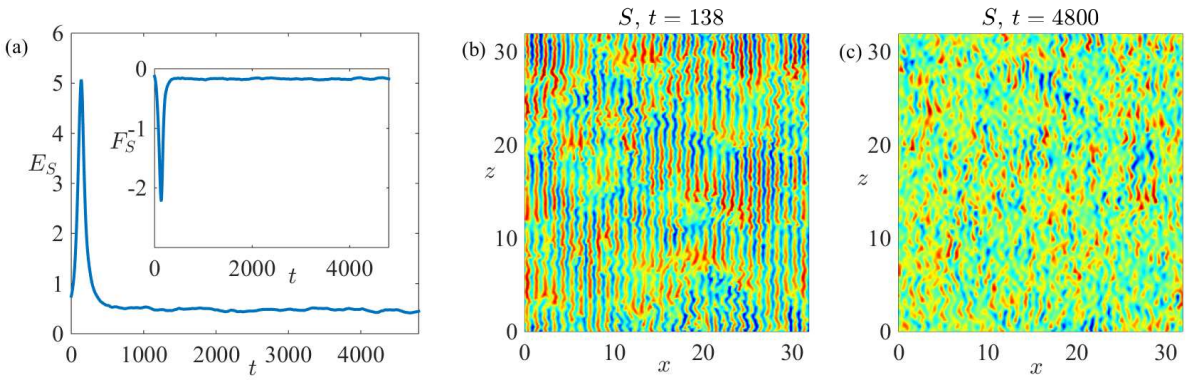

Figure 3: Results from a large-domain simulation. (a) Evolution of the total energy (main panel) and salinity flux (inset) with time. (b) The finger-dominanted state at $t = 138$. (c) The instantaneous statistically steady state at $t = 4800$. Distances are measured in units of the wavelength of the optimal mode.

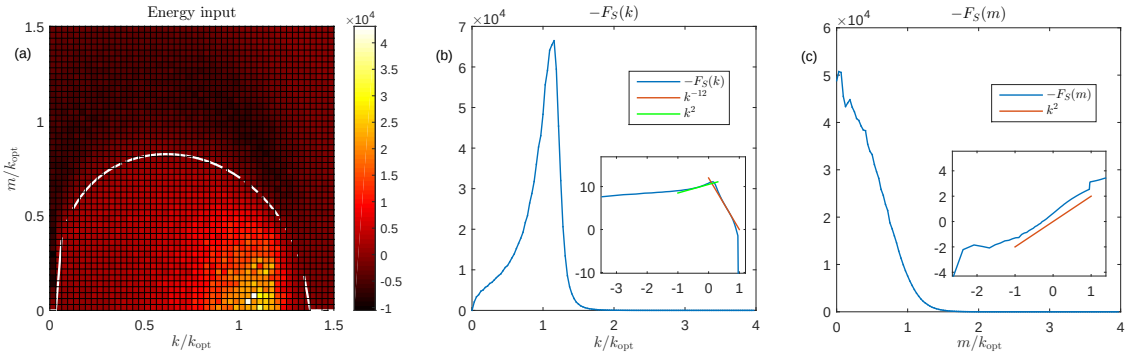

Figure 4: Spectral analysis of time-averaged saturate state (averaged over $t \in (3600, 6000)$). (a) The energy input at scales (k, m). (b,c) One-dimensional salinity flux spectra obtained by integrating the two-dimensional salinity flux spectrum $\hat{F}_S(k, m)$ over m and k, respectively; the insets show $\log(\hat{F}_S(k))$ vs $\log(k)$ and $\log(\log(\max\{\hat{F}_S(m)\}/\hat{F}_S(m)))$ vs $\log(k)$ to identify the power laws and Gaussian distribution. Here, due to symmetry only positive wavenumbers are presented.

mal horizontal wavenumber while dissipation involves both the resulting horizontal mean flow and small-scale structures.

In Fig. 4(b,c), we examine the flux spectrum defined as $\hat{F}_S = \widehat{\psi_x}\hat{S}^* + \widehat{\psi_x}^*\hat{S}$ with * denoting the complex conjugate. It is important to note that this quantity captures the net salinity flux across the full domain; it plays a role similar to that of the energy spectrum. When integrated over the vertical wavenumber m, the horizontal flux spectrum $\hat{F}_S(k)$ exhibits a peak around the optimal wavenumber, indicating that finger structures dominate the salinity flux; the behavior of the salinity flux can thus be used to identify the salt-finger regime. Different k dependence is observed on either side of $k = \pm k_{\rm opt}$ (owing to normalization $k_{\rm opt} = 1$): when $k < k_{\rm opt}$ we observe a k^2 scaling while a k^{-14} scaling is observed for $k > k_{\rm opt}$ (see Fig. 4(b,c), insets). When integrated over k, the vertical flux spectrum $\hat{F}_S(m)$ has a Gaussian distribution instead, with zero mean and variance ≈ 0.5, implying that the characteristic vertical salt-finger scale is twice of the optimal wavelength.

5 Conclusion

In this paper, we derived two reduced models, Eqs. (3) and (4), that describe salt-finger convection in the limit of small diffusivity ratio and large flux ratio. The reduced model (4) has a prognostic-diagnostic form and provides a concise understanding not only of linear instability, but of the role of the temperature in generating large-scale damping and the resulting energy budget as well. We provided detailed results for $\mathrm{Ra} = 1.1$ and different domain sizes and confirmed that our reduced model captures both linear and nonlinear properties of the primitive equations, including both the linear stability conditions, the conditions for secondary instability and the subsequent saturation. In large domains we identified the salinity flux spectrum as a good diagnostic for salt-finger convection: the horizontal flux spectrum exhibits power-law dependence on either side of the optimal wavenumber while the vertical flux spectrum has a Gaussian distribution with zero mean.

Acknowledgement: This work was supported by the National Science Foundation under grant No. DMS-1317666.

References

Holyer, J. Y. (1984). The stability of long, steady, two-dimensional salt fingers. *J. Fluid Mech.*, 147:169–185.

Julien, K. and Knobloch, E. (2007). Reduced models for fluid flows with strong constraints. *J. Math. Phys.*, 48:065405.

Proctor, M. R. E. and Holyer, J. Y. (1986). Planform selection in salt fingers. *J. Fluid Mech.*, 168:241–253.

Radko, T. (2010). Equilibration of weakly nonlinear salt fingers. *J. Fluid Mech.*, 645:121–143.

Radko, T. and Smith, D. P. (2012). Equilibrium transport in double-diffusive convection. *J. Fluid Mech.*, 692:5–27.

Schmitt, R. W. (1994). Double diffusion in oceanography. *Annu. Rev. Fluid Mech.*, 26:255–285.

Shen, C. Y. (1995). Equilibrium salt-fingering convection. *Phys. Fluids*, 7(4):704–717.

Stern, M. E. (1960). The 'salt-fountain' and thermohaline convection. *Tellus*, 12:172–175.

Stern, M. E. (1969). Collective instability of salt fingers. *J. Fluid Mech.*, 35:209–218.

Stern, M. E. and Simeonov, J. (2005). The secondary instability of salt fingers. *J. Fluid Mech.*, 533:361–380.

Traxler, A., Stellmach, S., Garaud, P., Radko, T., and Brummell, N. (2011). Dynamics of fingering convection. Part 1 small-scale fluxes and large-scale instabilities. *J. Fluid Mech.*, 677:530–553.

Turner, J. S. (1974). Double diffusive phenomena. *Annu. Rev. Fluid Mech.*, 6:37–54.